communications earth & environment

Article

A Nature Portfolio journal

https://doi.org/10.1038/s43247-026-03330-4

Drought propagation as a nonlinear amplifier of ecohydrological damage

Check for updates

Zhuoran Qu [1,2,3], Xiaoyan Li [1,2] ✉, Josep Peñuelas [3,4], Deliang Chen [5], Chiyuan Miao [1], Yuanhong Deng [1,2], Fangzhong Shi [1,2] & Wenqi Li [6]

Meteorological drought can propagate to soil and ecological droughts, triggering cascading disruptions in ecosystem functioning. However, whether the ecohydrological damage—the sum of standardized vegetation greenness and soil moisture losses—is disproportionately amplified through drought propagation has not been systematically assessed. Using multiple global datasets, we found that ecohydrological damage reached 162% to 310% of the initial meteorological drought intensity. Once meteorological drought intensity exceeded the standardized threshold of 2.18, ecohydrological damage escalated nonlinearly. Externally, soil and ecological droughts were more sensitive to precipitation deficits and potential evapotranspiration surpluses, respectively. Internally, vegetation–soil feedbacks promoted the propagation from soil to ecological drought, while dampened the reverse process, resulting in the greatest ecohydrological damage along the meteorological–soil–ecological drought propagation pathway. Declining ecosystem resilience and increasing climate variability may exacerbate future drought propagation and its damage. These insights are critical for advancing early warning systems and mitigating cascading drought losses.

Drought is one of the most prevalent and devastating natural disasters[1], leading to a global economic loss of at least $124 billion over two decades[2]. In the context of global warming, more frequent and severe droughts have posed tremendous challenges to environmental stability and sustainable development[3]. Drought can propagate through the hydrological cycle, affecting different components of ecosystems. Typically, it begins as a meteorological drought caused by reduced precipitation or increased potential evapotranspiration. This initiates a chain reaction in which reduced water input and higher evaporative demand generate water deficits in the soil and vegetation, resulting in soil drought and ecological drought. This cascading process is known as drought propagation. Land–atmosphere feedbacks can either amplify or attenuate the duration and severity of these water deficits[4]. Moreover, multiple components of the ecosystem are progressively damaged as drought propagates[5], leading to escalating destruction. Catastrophic ecosystem collapse and cascading functional degradation may be triggered through amplification of drought damage[6,7]. Therefore, elucidating the propagation characteristics and mechanisms across different droughts is crucial prerequisite for improving drought monitoring capabilities and mitigating drought cascade losses.

Traditionally, droughts are classified into meteorological, agricultural, hydrological, and socio-economic types[8]. Previous studies have documented the propagation characteristics, propagation risks, and driving factors across these four types of droughts[9–11]. However, this conventional human-centered classification of drought cannot fully capture the responses of organisms or ecosystems to water scarcity conditions. Droughts can cause plant cell dehydration, leaf drop, mortality, biodiversity reduction and soil degradation[5,12], which not only directly undermines the ecological balance and carbon sequestration function of ecosystems, but also increases their vulnerability to climate variability and human disturbances[13,14]. Ignoring these ecological consequences of water stress and its knock-on effects can seriously undermine environmental health and human well-being through the loss of vital ecosystem services.

In response, the concept of ecological drought has been proposed in recent years to describe drought-induced ecological impacts[15,16]. Within this framework, meteorological, soil and ecological drought refer to water deficits in the atmosphere, soil, and vegetation, respectively. Propagation among these three types of droughts reflects the dynamic transfer of water deficit signals through the soil–plant–atmosphere continuum (SPAC)[6,17]. Mechanistic decoding of these processes will enable a holistic assessment of ecohydrological damage during drought.

Several studies have suggested the complex interactions among meteorological, soil, and ecological droughts. Meteorological drought

[1]State Key Laboratory of Earth Surface Processes and Disaster Risk Reduction, Faculty of Geographical Science, Beijing Normal University, Beijing, China. [2]School of Natural Resources, Faculty of Geographical Science, Beijing Normal University, Beijing, China. [3]CREAF, Cerdanyola del Vallès, Barcelona, Catalonia, Spain. [4]CSIC, Global Ecology Unit CREAF-CSIC-UAB, Bellaterra, Barcelona, Catalonia, Spain. [5]Department of Earth System Science, Tsinghua University, Beijing, China. [6]College of Urban and Environmental Sciences, Peking University, Beijing, China. ✉e-mail: xyli@bnu.edu.cn

reduces water supply to the soil and increases evaporative demand via high vapor pressure deficit, intensifying soil moisture loss[18]. Severe soil water shortage can then limit plant water uptake and physiological activity, triggering ecological drought. Interestingly, vegetation may initially show high greenness and photosynthesis under clear skies during early drought stages[19], rapidly depleting soil water. Meanwhile, reduced evapotranspiration from soil and vegetation during drought can feed back to intensify meteorological drought[20]. Despite these findings, few quantitative studies have systematically assessed the full propagation pathways, timing, and ecohydrological damage of meteorological droughts progressing into soil and ecological droughts. Moreover, little attention has been paid to the differing effects of droughts caused by precipitation deficits versus those driven by excess potential evapotranspiration. The bidirectional feedback between soil and ecological drought also remains understudied. As a result, key knowledge gaps remain regarding how diverse external drivers and internal interactions influence drought propagation and its damage.

Here, we define ecohydrological damage as the sum of leaf area index (LAI) and soil moisture (SM) losses during drought, which is equal to the sum of soil and ecological drought intensity. From the perspectives of propagation characteristics, external drivers, and internal interactions, this study systematically investigates how meteorological drought propagates to soil and ecological drought. Specifically, we aim to: (1) quantify the propagation time, propagation intensity and resulting ecohydrological damage along different propagation pathways; (2) examine how meteorological droughts of distinct origins—precipitation deficit versus potential evapotranspiration surplus—affect drought propagation; and (3) evaluate how soil–vegetation feedback modulates drought propagation and its ecohydrological damage. The outcomes of this study provide vital insights for adapting to the growing challenges of exacerbated drought propagation and increased flash droughts under climate change[11,21].

Results

Drought propagation characteristics along different pathways

The de-trended monthly PPET (precipitation minus potential evapotranspiration), SM, and LAI were used as indicators of meteorological (M), soil (S), and ecological drought (E), respectively (see "Methods"). Based on the sequence of drought onset, we identified five propagation pathways from M to S and E (Fig. 1). At the global scale, the frequency of M–E was the highest, followed by M–S, suggesting greater vulnerability of vegetation to M than soil. Among the longer three-step propagation chains, the M–S–E pathway occurred most frequently, accounting for 19% of global drought propagations. In contrast, M–E–S and M–S&E were less common, comprising only 8% and 7% of propagations, respectively. This indicates that when both S and E were triggered by M, the vegetation usually experienced droughts later than the soil. From the hyper-arid to humid zones, there were no obvious differences in the relative proportions of these pathways.

We further analyzed the characteristics of drought propagation along all pathways except for M–S&E, for which the sequence of S and E was indeterminate within the same month. Compared to M–S, the M–E pathway had a lower trigger condition but a longer propagation time (Fig. 2a, b), supporting the earlier observation that M–E was more frequent and that S usually preceded E when both were triggered. Across all pathways, the duration and intensity of S or E were not less than those of M (Fig. 2c, d), highlighting the prolonged drought duration and amplified drought severity during the propagation. In long-chain propagations of M–S–E and M–E–S, drought intensity generally declined from the second to the third node, with median reductions of 23%–35%. However, 17% of M–S–E and 18% of M–E–S exhibited sustained increases in drought intensity during propagation. Among all pathways, M–S–E led to the most severe ecohydrological damage, with the combined intensity of S and E reaching 3.10 times that of M, followed by M–E–S, with a 2.65-fold amplification. Damage of these long-chain propagations exceeded that of short-chain propagations (M–S and M–E), as drought damage at the second node was already comparable to or even greater than that of short-chain propagations, with further amplification as drought propagated to the third node (Fig. 2d).

The drought propagation characteristics derived using LAI as the indicator of E were generally consistent with those based on gross primary productivity (GPP), net ecosystem exchange (NEE), and solar-induced chlorophyll fluorescence (SIF), particularly GPP and SIF (Supplementary Figs. S2–4). Across all pathways, E intensity exceeded the initial M intensity, with the M–S–E pathway exhibiting the greatest ecohydrological damage—3.1, 2.8, and 2.9 times the M intensity for GPP, NEE, and SIF, respectively. These indicate that drought propagation also caused amplified impairments in carbon assimilation, carbon balance, and photosynthetic efficiency.

Nonlinear amplification of ecohydrological damage during drought propagation

As drought propagated from M to S and E, propagation time and ecohydrological damage exhibited a nonlinear shortening and amplification with increasing intensity of M, respectively. Specifically, the propagation time initially declined rapidly, followed by an abrupt downward jump at the threshold (M intensity = 3.08) (Fig. 3a), with the magnitude of the jump diminishing with increasing bin count (Supplementary Fig. S5). Although the post-breakpoint slope was gentler, drought has transitioned from an initial slow propagation phase to a markedly faster one. Besides, the total ecohydrological damage remained relatively constant when M intensity was below 2.18. Beyond this breakpoint, damage increased sharply, with the slope of the fitted curve rising from −0.09 to 0.68 (Fig. 3b), indicating that stronger M will lead to greater ecohydrological damage through drought propagation. Sensitivity tests indicated that the values of breakpoint varied slightly with the number of bins, while the significance remained at $P < 0.001$ (Supplementary Fig. S5). Both increases in P deficit and PET surplus during M shortened propagation time, and ecohydrological damage rose sharply beyond the breakpoints of 2.15 and 1.49 for cumulative P deficit and PET surplus, respectively (Supplementary Fig. S6). Globally, drought propagation amplified the ecohydrological damage in 99% of affected places, with M triggering damages that systematically exceeded its original intensity. Notably, 77% of these places exhibited at least a twofold amplification of ecohydrological damage compared to the initial M intensity, and 30% experienced a more than threefold exacerbation, which occurred mainly in mid- to high latitudes of North America, northern South America, and humid and dry sub-humid regions across Eurasia.

Lag-one autocorrelation (AC1) helps explain this amplification of ecohydrological damage. Pairwise comparisons revealed that AC1 values of PPET were significantly lower than those of SM and LAI ($P < 0.001$), with global medians of 0.11, 0.79, and 0.54, respectively (Supplementary Fig. S7). This indicates that the atmosphere adjusted and recovered rapidly from drought, whereas soil and vegetation exhibited markedly lower resilience and thus much slower recovery, which led to the amplified damage. Moreover, the AC1 values of SM and LAI were negatively correlated with drought propagation time ($P < 0.001$) and positively correlated with intensity propagation ratio ($P < 0.001$), suggesting that lower resilience will accelerate and exacerbate drought propagation (Supplementary Table S1).

Attribution of drought propagation variability to external meteorological drivers

Precipitation (P) deficits and potential evapotranspiration (PET) surpluses are two distinct drivers of meteorological drought. Meanwhile, SM and LAI serve as the primary diagnostic variables for soil and ecological droughts, respectively. Therefore, we assessed the response lag and propagation efficiency from P and PET to SM and LAI (i.e., P → SM, PET → SM, P → LAI and PET → LAI), to investigate variations in drought propagation driven by different meteorological factors. Relative propagation efficiency, e.g., P → SM | PET → SM, compares the propagation efficiencies of P → SM and PET → SM; value > 0 indicates P → SM propagates more efficiently, while value < 0 indicates PET → SM does. SM responded immediately to changes in P (0-month lag), but with a delayed response of 0–7 months to PET (Fig. 4a). Except in the hyper-arid zone where the lag times were similar, SM responded faster to P than to PET. Across all levels of aridity, P → SM showed consistently higher propagation efficiency than PET → SM

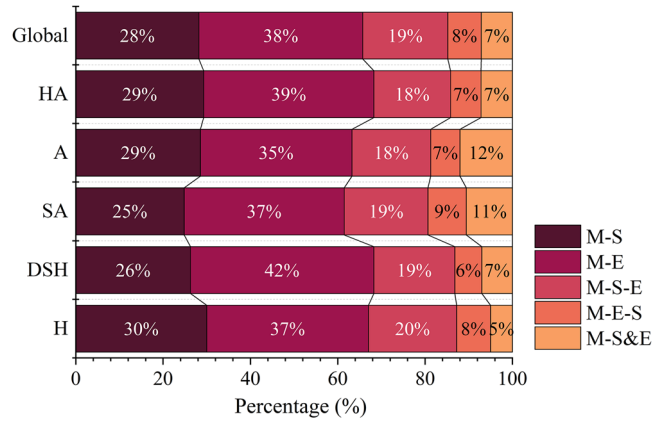

Fig. 1 | Frequencies of five drought propagation pathways from meteorological to soil and ecological drought. M, S, and E represent meteorological, soil, and ecological drought, respectively. M–S and M–E indicate that only one secondary drought (S or E) followed M, without triggering the other. M–S&E denotes the case in which S and E began in the same month after M. HA, A, SA, DSH, and H represent hyper arid, arid, semi-arid, dry sub-humid, and humid zones, respectively (Supplementary Fig. S1).

(Fig. 4b), highlighting P as the dominant driver for SM variability. For LAI, the response to P lagged behind that to PET by 0–2 months, again with the exception of the hyper arid zone. In hyper-arid and arid zones (aridity index < 0.2), the propagation efficiency of P → LAI and PET → LAI was similar. As the humidity increased, PET became more efficient than P in driving changes in LAI. Overall, P and PET were the dominant meteorological factors for SM and LAI, respectively. This implied that the M–S–E drought propagation pathway was predominantly driven by P anomalies, with the water deficit signal transmitted mainly along P → SM → LAI; whereas the M–E–S was predominantly driven by PET anomalies, with the water deficit signal transmitted mainly along PET → LAI → SM. Furthermore, P → SM always demonstrated shorter lag time and higher propagation efficiency than PET → LAI along the entire aridity gradient. This supports the findings in Fig. 2 that the M–S pathway exhibited a shorter propagation time than M–E, and that the M–S–E pathway caused more severe ecohydrological damage than M–E–S.

Modulation of drought propagation by internal soil–vegetation feedbacks

To investigate the role of internal feedbacks during drought propagation, we analyzed how antecedent SM and LAI influenced subsequent drought severity. For propagation of M–S–E, we examined how SM between the onset of S and E (referred to as antecedent SM) modulated E intensity.

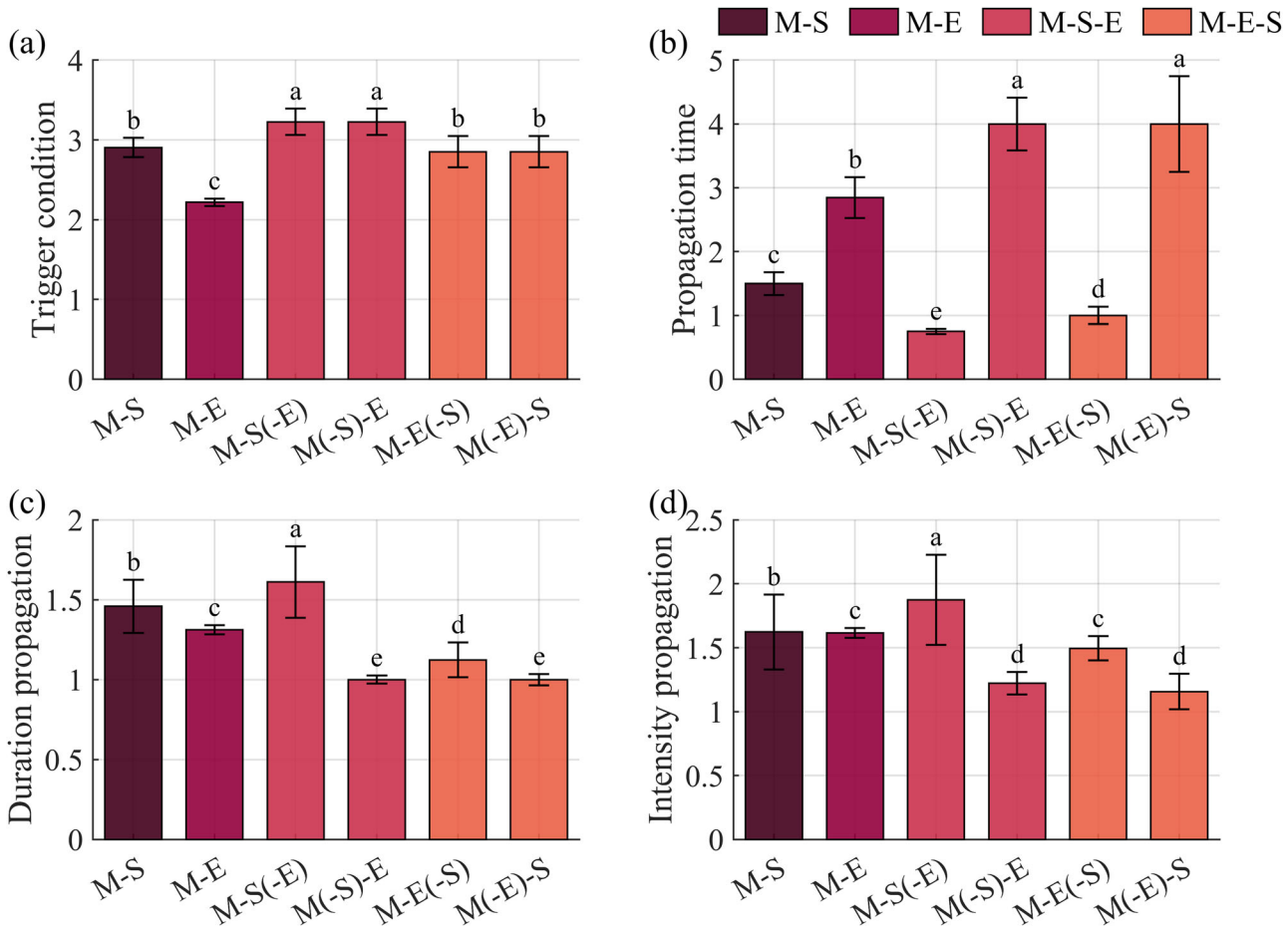

Fig. 2 | Drought propagation characteristics along different pathways. The characteristics include **a** trigger condition, **b** propagation time (in months), **c** duration propagation ratio and **d** intensity propagation ratio from meteorological drought (M) to soil drought (S) and ecological drought (E). Taking the long-chain propagations of M–S–E as an example, M–S(–E) represents the propagation characteristics from M to S, while M(–S)–E represents that from M to E, with the parenthesized nodes excluded from the analysis. The four bar colors in the legend indicate the four drought propagation pathways. The duration (or intensity) propagation ratio is calculated as the duration (or intensity) of S or E divided by that of M. The bars represent the global medians, and error bars represent ±0.5 IQR (interquartile range) of medians across five climatic zones. Bars labeled with different letters indicate statistically significant differences based on Wilcoxon signed-rank tests (paired by spatial location, $P < 0.05$).

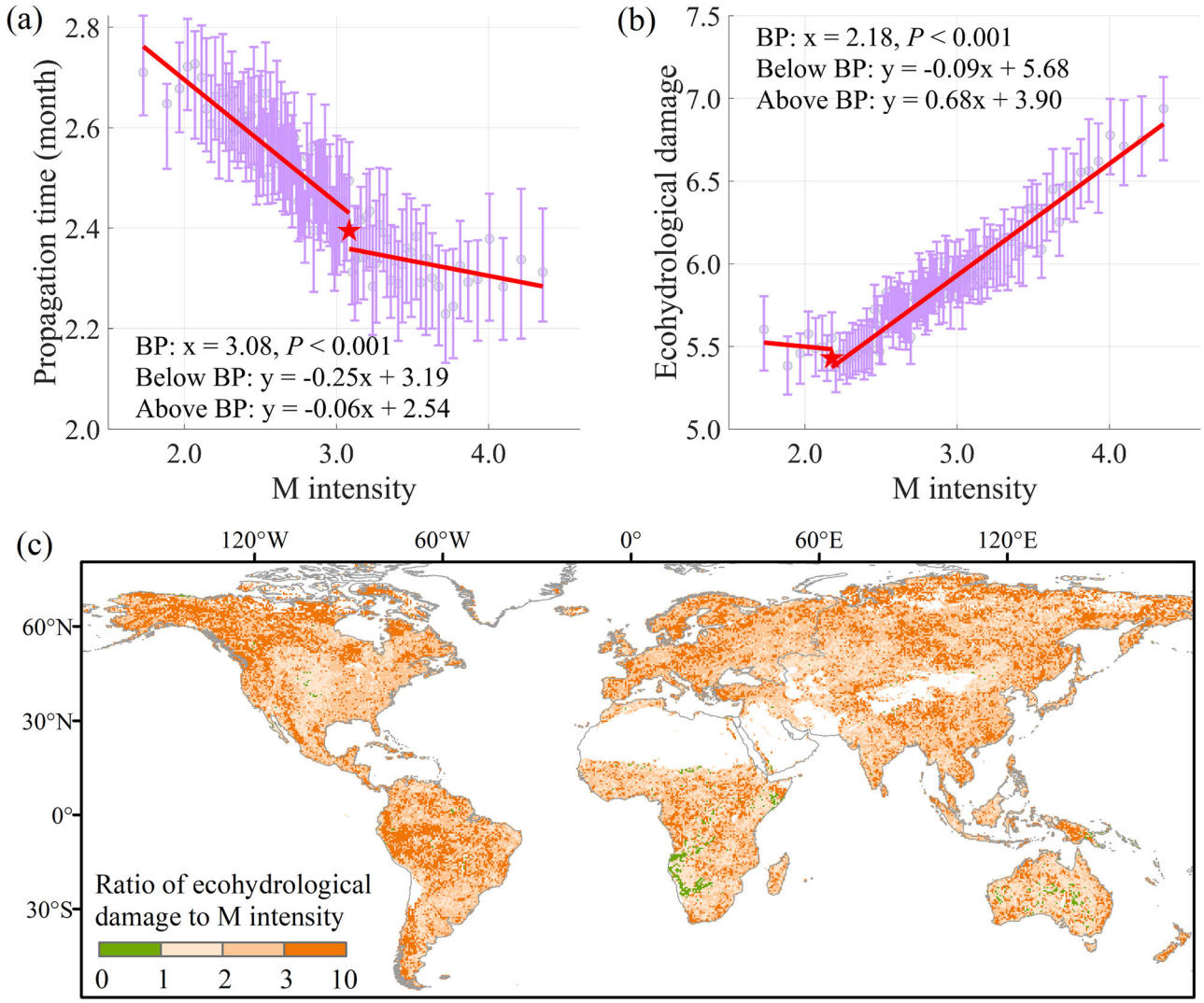

Fig. 3 | Nonlinear amplification of ecohydrological damage during propagation from meteorological to soil and ecological drought. Variations in **a** propagation time and **b** total ecohydrological damage with increasing meteorological drought (M) intensity. Purple dots and error bars represent the median and 95% confidence interval for each bin, respectively (see "Methods"). Red pentagrams represent the breakpoints (BPs) in the medians, with their y-coordinates determined by averaging the two predicted values on either side of each BP. Red lines represent fitted curves for medians below and above the BPs. The values and significance of the BPs, together with the regression equations, are shown in the lower-left corner of **a** and the upper-left corner of **b**. **c** The spatial pattern of ecohydrological damage per unit M intensity, with orange and green indicating areas where ecohydrological damage is greater than or less than M intensity, respectively.

And for M–E–S, we examined how LAI between the onset of E and S (referred to as antecedent LAI) modulated S intensity. A partial correlation analysis, controlling for M intensity, showed a significant negative correlation between antecedent SM and E intensity (Spearman's $\rho = -0.11$, $P < 0.001$), suggesting that lower antecedent SM intensified E. In contrast, there was a significant positive correlation between antecedent LAI and S intensity (Spearman's $\rho = 0.02$, $P < 0.001$), indicating that lower antecedent LAI reduced water consumption and somewhat buffered S development. These evidences suggest that S promoted the transmission of water deficits in M–S–E, while E blocked the transmission of water deficits in M–E–S.

Furthermore, we assessed the mediation effect of antecedent SM in the propagation of M–S–E (Fig. 5), which transmitted the water deficits mainly along P → SM → LAI, and explored the mediation effect of antecedent LAI in M–E–S, which transmitted the water deficits mainly along PET → LAI → SM. In P → SM → LAI, although no significant direct effect of P on LAI was detected, P deficits reduced LAI indirectly through SM decline, with a mediation effect of 0.02 ($P < 0.001$), accounting for 66% of the total effect. Besides, in PET → LAI → SM, PET surpluses exhibited a significant dual effect ($P < 0.001$) on SM: a strong negative direct effect through increased evaporative loss, and a weaker positive mediation effect via reduced LAI and thus reduced transpiration. These findings further demonstrate that S tends to further exacerbate E in M–S–E, while E tends to mitigate S and dampen drought propagation in M–E–S to some extent, which explains why M–S–E led to greater ecohydrological damage than M–E–S (Fig. 2d) from the perspective of internal feedbacks.

Discussion

Meteorological drought (M) characterized by insufficient P and high PET, can lead to reduced SM and suppressed plant growth, evolving into soil drought (S) and/or ecological drought (E) through the propagation of water deficits along the hydrological cycle[6,22]. E exhibited lower trigger condition and greater vulnerability to M than S (Figs. 1 and 2). This may be attributed to moisture inputs via lateral flow and hydraulic redistribution, along with reduced soil evaporation from canopy shading, which together buffer the negative impacts of M on SM[23–25]. But when E and S were both triggered, S usually started earlier because the response lags for P → SM and PET → LAI were 0 month and 1–4 months, respectively (Fig. 4a).

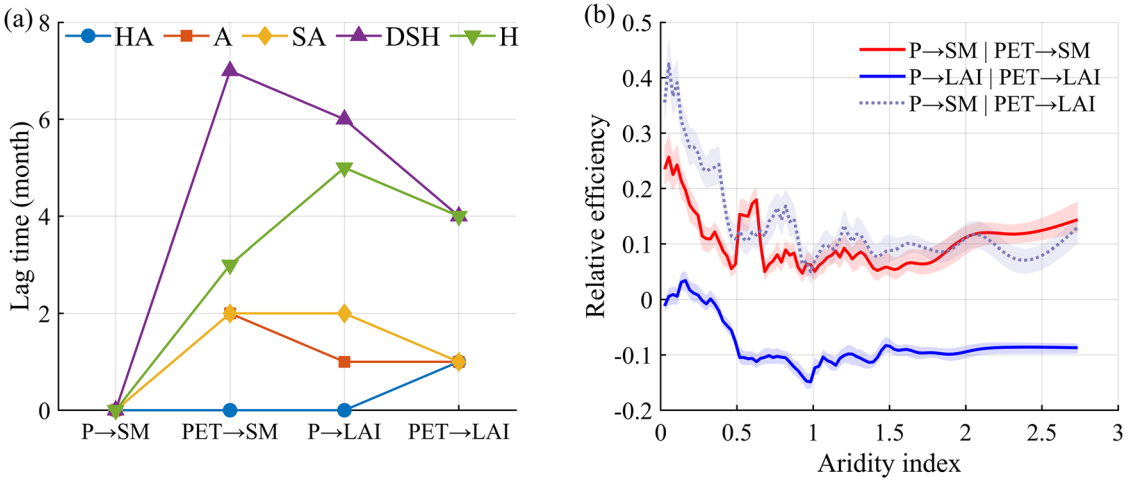

Fig. 4 | Propagation from meteorological droughts of different origins to soil and ecological droughts. Meteorological drought origin is classified into two types of precipitation (P) and potential evapotranspiration (PET). **a** Lag time in the response of leaf area index (LAI) and soil moisture (SM) to P and PET across different climatic zones. HA, A, SA, DSH, and H represent hyper arid, arid, semi-arid, dry sub-humid, and humid zones, respectively (Supplementary Fig. S1). **b** Relative propagation efficiency between variable pairs. Shaded areas represent 95% confidence intervals estimated using the bootstrapped method with 1,000 replications.

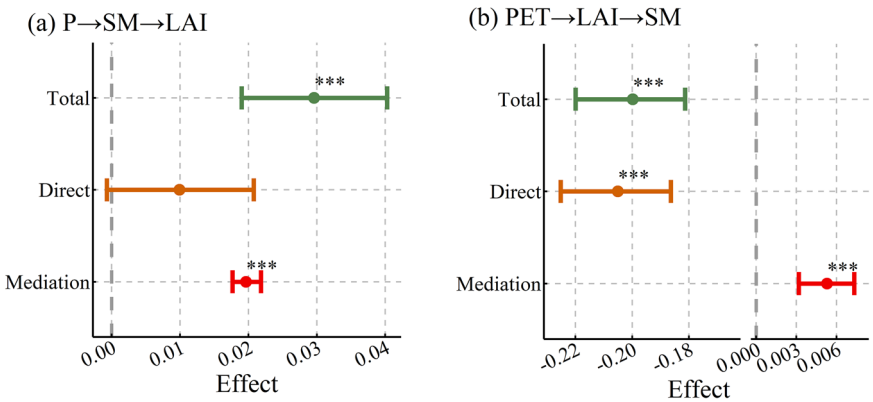

Fig. 5 | Modulation of soil–vegetation feedbacks in drought propagation. When water deficits propagate, the direct effects, mediation effects, and total effects in the transmission **a** along precipitation→soil moisture→leaf area index (P → SM → LAI) and **b** along potential evapotranspiration→leaf area index→soil moisture (PET → LAI → SM) are shown. Error bars represent 90% confidence intervals. $x = 0$ is highlighted with a bolded gray dashed line. In **b**, the x-axis features a discontinuity between −0.165 and 0 to resolve scale disparities while maintaining data integrity. *** indicates $P < 0.001$.

Unlike previous studies that mainly focused on pairwise drought propagation (e.g., from meteorological to agricultural[26] or hydrological drought[17,27]), this study adopts a systemic, long-chain perspective to unravel the cascades of S and E after the onset of M, and reveals the generalized amplification of ecohydrological damage during drought propagation. For the propagation pathways of M–S, M–E, M–S–E, and M–E–S, the total ecohydrological damage reached 162%, 162%, 310%, and 265% of the original M intensity, respectively (Fig. 2d). On the one hand, this is due to the lengthening of drought duration. The drought durations of S and E along these pathways were 1.46, 1.31, 2.61, and 2.12 times longer, respectively, than M (Fig. 2c). This is consistent with prior studies, which claimed that the duration of drought was prolonged during its propagation from the atmosphere to the soil[18]. On the other hand, the peak intensities of S and E ranged from 0.97 to 1.23 times that of M (Supplementary Fig. S8). Stronger M triggered disproportionately higher damage (Fig. 3b). These suggest that drought propagation from M to S and E acts as a nonlinear amplifier of ecohydrological damage. Coarse spatial resolution may compress spatial heterogeneity of the result (Supplementary Fig. S9). We have adopted the finest version of the current datasets, and expect production of data with higher spatial resolution and accuracy.

Ecosystem resilience has declined globally since the early 2000s[28,29], with over 60% of terrestrial ecosystems shifting from rising to falling resilience since 1982[30]. This is attributed to increasing precipitation variability, decreasing vegetation cover, increasing temperature variability and increasing average temperature[30]. Projected increases in precipitation variability are expected to further weaken resilience[31]. This highlights the increase in drought sensitivity and loss of ecosystem stability, suggesting that the amplification effects of drought propagation on ecohydrological damage will be further enhanced in the future (Supplementary Table S1).

Drought propagation is shaped by both external meteorological drivers and internal soil–vegetation feedbacks. It was demonstrated that rising PET has increased the frequency of agricultural droughts more profoundly than hydrological droughts[32]. In the Middle and Lower Reaches of the Yangtze River of China, hydrological droughts were more sensitive to rainfall deficits, while agricultural droughts were more sensitive to elevated evaporation[33]. In this study, P and PET were considered as two independent contributors to drought, representing low water supply and large water loss, respectively. We found that the meteorological drought driven by P would propagate to soil more rapidly and efficiently than to vegetation, whereas drought driven by PET would exhibit faster and more efficient propagation to vegetation than to soil. This is because P deficits first reduce root-zone SM and lower soil water potential, thereby restricting root water uptake and subsequently transmitting the water deficits to leaves, which delays the impact on LAI[34]. Furthermore, PET was driven by temperature in arid regions and by net radiation in humid regions, with relative humidity and wind speed as the third and fourth most influential factors (Supplementary Fig. S10). Under

global warming, higher temperature and net radiation elevated saturated vapor pressure and energy supply, which enhanced PET and resulted in a faster rise in the frequency of droughts driven by PET surplus than those driven by P deficit in some places[33]. This may expose vegetation to earlier and stronger damage in drought propagation.

Once drought propagates from atmosphere to land, soil–vegetation feedbacks regulate the severity of drought. Our bootstrap mediation analysis confirmed facilitation in drought propagation of M–S–E and damping in propagation of M–E–S (Fig. 5). During M–S–E, low SM and high LAI typically co-occur when S begins but E has not yet occurred (Fig. 6). Under such circumstances, low SM limits water supply, while high LAI reduces precipitation recharge through canopy interception and generates massive water depletion through root water uptake and transpiration[19,35]. These will exacerbate S and E, and cause greater drought damage. Contrastingly, during M–E–S, low LAI and high SM co-occur when E begins but S has not yet occurred. At this stage, the ecosystem exhibits low water consumption and a relatively adequate water supply[25], reducing the severity of drought propagation. These feedbacks help explain why M–S–E pathway tends to cause more ecohydrological damage than M–E–S.

The key findings and underlying mechanisms were applicable throughout the year (Supplementary Figs. S11–13). But autumn exhibited the highest drought intensity propagation ratio, likely due to its lower trigger condition (Supplementary Fig. S11a, d). And the modulation effects of soil–vegetation feedback on drought propagation were maximized in winter (Supplementary Fig. S13), resulting in the largest disparity in intensity propagation ratio of 0.45 between M–S–E and M–E–S pathways, compared with 0.25, 0.33, and 0.19 in spring, summer, and autumn, respectively.

Climate warming and anthropogenic impacts have exacerbated global droughts[3,36]. Future drought events will be longer, more severe, and more destructive[37]. In particular, the world is experiencing a transition to flash droughts[21]. Such rapidly intensifying droughts pose remarkable challenges for drought monitoring and forecasting. With declining resilience and enhanced meteorological drought, drought propagation may become faster and cause greater ecohydrological damage in the future (Fig. 3). Our findings provide critical early warning information on drought cascades, and are instructive for drought monitoring and management to mitigate the catastrophic damages on ecohydrology and socio-economics.

Conclusions

Drought propagated from meteorological to soil and ecological droughts along various pathways, but the ecohydrological damage consistently exceeded the initial meteorological drought intensity. This amplification was primarily driven by the lower resilience of soil and vegetation compared to the atmospheric adjustment capability, leading to prolonged drought duration and increased peak intensity during propagation. Notably, when meteorological drought intensity surpassed certain thresholds, propagation accelerated and damage escalated rapidly. Among external drivers, P deficits and PET surpluses primarily drove soil and ecological droughts, respectively. However, P-driven droughts tended to propagate more quickly and efficiently to soil than PET-driven droughts to vegetation. Internally, soil–vegetation feedbacks had a facilitating effect on M–S–E propagation and a damping effect on M–E–S propagation. Consequently, the M–S–E resulted in the greatest ecohydrological damage among all pathways. The nonlinear amplification of ecohydrological damage during drought propagation is expected to worsen in the future, due to declining ecosystem resilience and increasing meteorological variability. These trends highlight the growing vulnerability of ecosystems under future climate conditions and the need for enhanced monitoring and adaptive management strategies.

Materials and methods

Data

The CRU TS (Climatic Research Unit gridded Time Series) dataset provides global climate data since 1901 at a 0.5° spatial resolution, which is fully validated and widely used[38]. CRU TS is generated by interpolating monthly

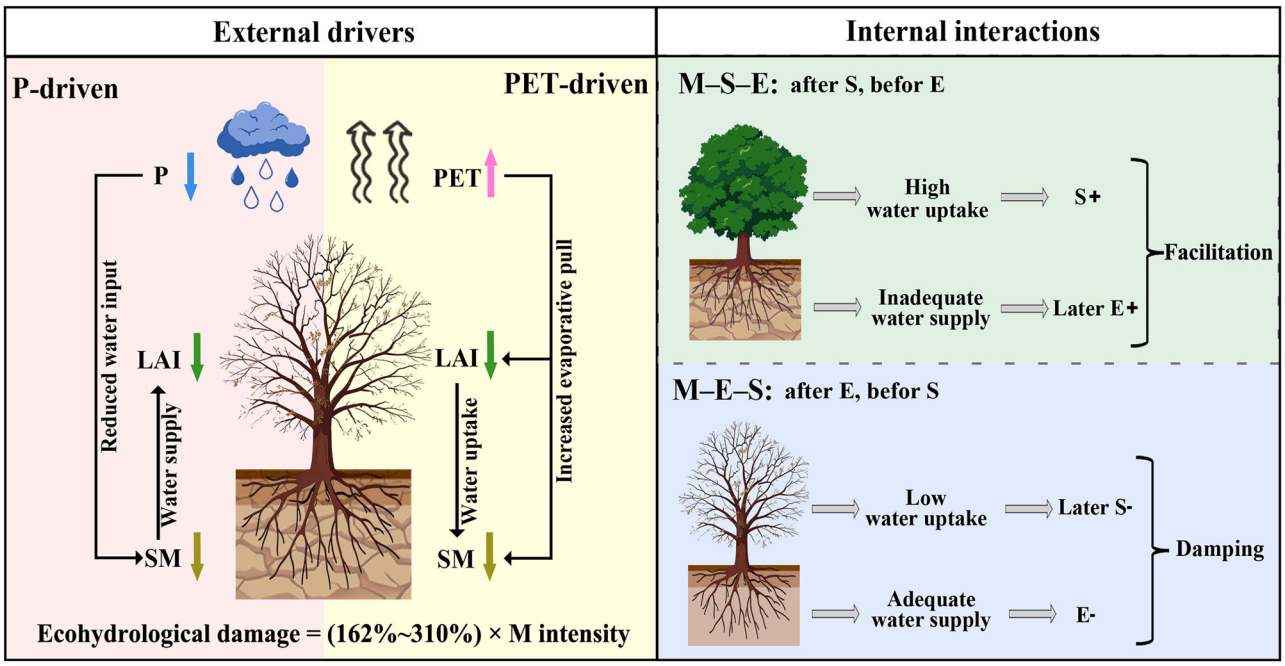

Fig. 6 | Conceptual map of propagation from meteorological to soil and ecological drought. M, S, and E represent meteorological, soil, and ecological drought, respectively. P, PET, LAI, and SM represent precipitation, potential evapotranspiration, leaf area index, and soil moisture, respectively. Upward and downward colored arrows indicate increases and decreases in the variables, respectively. In terms of external drivers, the left panel illustrates how P and PET affect SM and LAI through different mechanisms, ultimately leading to ecohydrological damage that is 162%–310% of the original M intensity. In terms of internal interactions, the right panel contrasts soil–vegetation feedbacks between the M–S–E and M–E–S pathways: low antecedent SM during M–S–E provides limited water, exacerbating subsequent LAI reduction and facilitating drought propagation, whereas low antecedent LAI during M–E–S reduces transpiration, conserving SM and dampening the drought signal; consequently, M–S–E produces the greatest ecohydrological damage among all pathways. Some elements (i.e., tree and cloud) were created with BioGDP.com[61].

climate anomalies from an extensive network of weather stations using angular-distance weighting, which enhances interpolation efficiency and accuracy. We used monthly P and PET to represent the atmospheric water supply and demand, respectively. The difference between them (PPET = P − PET) was used as an indicator of atmospheric water balance[39].

The Global Land Evaporation Amsterdam Model (GLEAM) estimates SM using a multi-layer running water balance model and assimilates satellite-derived surface SM into the soil profile to reduce errors[40]. The fourth-generation GLEAM provides a continuous daily dataset from 1980 to 2023 at a spatial resolution of 0.1°, which has been successfully validated by in situ ecosystem measurements and widely used in hydrological, climatic, and ecological studies. We used root-zone SM to represent the soil moisture condition.

LAI, with clear biophysical meaning, is an efficient indicator for capturing vegetation dynamics. The fourth-generation Global Inventory Modeling and Mapping Studies LAI product (GIMMS LAI4g)[41] provides global half-month LAI data from 1982 to 2020, with a spatial resolution of 1/12°. It was produced using a back propagation neural network (BPNN) and a data consolidation method, and it has demonstrated overall higher accuracy and less underestimation in comparison to other mainstream datasets[42]. We derived monthly LAI by averaging the two half-monthly values.

We also used GPP, NEE, and SIF as supplementary indicators of LAI. GPP and NEE were derived from the Breathing Earth System Simulator version 2.0 (BESSv2.0), a coupled-process model with demonstrated reliability, providing daily carbon fluxes at a 0.05° spatial resolution since 1982[43]. Besides, to extend observations from the TROPOspheric Monitoring Instrument (TROPOMI), machine learning algorithms have been employed to generate the reconstructed TROPOMI SIF (RTSIF) dataset, which spans 2001–2020 at a 0.05° spatial resolution and 8-day temporal resolution. SIF from this dataset has been validated as a useful proxy of terrestrial photosynthesis[44,45].

ERA5-Land is a reanalysis dataset providing a consistent representation of land variables since 1950 at a 0.1° spatial resolution[46,47], including air temperature, dew point temperature, air pressure, u- and v-component wind speeds, and net radiation. Relative humidity was calculated from air temperature, dew point temperature, and air pressure[48]. Wind speed was derived from the u- and v-component wind speeds as the square root of the sum of their squares.

The above data for 1982–2020, except that SIF was available only for 2001–2020, were extracted and further aggregated to a spatial resolution of 0.5° by mean aggregation to match each other. Additionally, the Global Aridity Index and Potential Evapotranspiration Database (Global-AI_PET) provides 30 arc-seconds global raster data for aridity index[49,50]. This index, where higher values indicate wetter conditions, was resampled to 0.5° resolution and used to classify the globe into hyper-arid (<0.03), arid (0.03–0.2), semi-arid (0.2–0.5), dry sub-humid (0.5–0.65), and humid (>0.65) zones (Supplementary Fig. S1).

Identification of drought propagation

This study focuses on meteorological droughts driven by P deficits and PET surpluses, as well as their subsequent impacts on SM and vegetation growth. Accordingly, the de-trended monthly PPET, SM, and LAI were used as indicators of meteorological, soil, and ecological drought, respectively. We first subtracted the monthly means from the original monthly data series, which removed the effect of the seasonal cycle[51]. The detrend function in MATLAB was then used to remove long-term trends from the de-seasoned data. Through the above steps, the de-trended series for PPET, SM and LAI were obtained, and their standard deviations (SDs) were used to reflect anomalies in these data. Specifically, months with meteorological, soil, and ecological drought were identified respectively when de-trended PPET, SM and LAI values fell below −1 SD of their own. Compared to conventional drought indices such as standardized precipitation evapotranspiration index (SPEI), this anomaly-based approach facilitates the separation of the independent contributions of P and PET to drought and removes the interference of seasonal cycles and long-term trends. In addition to LAI, GPP, NPP, and SIF were also employed to identify ecological drought. These types of vegetation indices align with the core concept of ecological drought and are widely used in its identification[52–54].

A meteorological drought event begins when de-trended PPET drops below −1 SD and ends after it remains above −1 SD for three consecutive months. After the meteorological drought onset, the soil drought (ecological drought) starts with a de-trended SM (LAI) < − 1 SD and ends with de-trended SM (LAI) > − 1 SD persisting for three consecutive months. A valid drought propagation needs to satisfy the following conditions: (1) soil and ecological droughts begin within 12 months after the onset of meteorological drought[9] and end within 3 years; and (2) no second meteorological drought event occur during soil and ecological droughts. Based on the occurrence sequence of meteorological drought (M), soil drought (S) and ecological drought (E), the drought propagation pathways were categorized into five types: M–S, M–E, M–S–E, M–E–S, and M–S&E. The M–S&E pathway was excluded from the subsequent calculation of propagation characteristics because it was unable to determine the sequence of S and E, despite their concurrent onset in a month.

The intensities of M, S, and E were calculated as the negative sums of de-trended PPET, SM, and LAI over the corresponding drought durations, respectively, which were standardized by their respective SDs. And the ecohydrological damage was represented by the sum of LAI and SM losses during drought, which is equal to the sum of S and E intensities. As for drought propagation characteristics, the trigger condition was quantified by the M intensity, and the propagation time was defined as the time lag between the onset of two drought types. The duration propagation ratio was calculated as the duration of S or E divided by that of M, while the intensity propagation ratio was calculated as the intensity of S or E divided by that of M.

Nonlinear amplification of ecohydrological damage

To explore how ecohydrological damage changes with increasing M intensity, we calculated mean ecohydrological damage and M intensity across the four pathways (M–S, M–E, M–S–E, and M–E–S) for each pixel, and sorted the data in the ascending order of M intensity and divided it into $\sqrt{n}/2$ bins (rounded to the nearest integer of 96), where n is the total number of data points. Data points with M intensity beyond $[Q_1 - 1.5\times IQR, Q_3 + 1.5\times IQR]$ were excluded, where Q_1 and Q_3 are the first and third quartiles, and IQR is the interquartile range ($IQR = Q_3 - Q_1$). Within each bin, median values of M intensity and ecohydrological damage were calculated, and the breakpoint in the median series was detected by a stegmented regression model using the chngpt package in R[55]. The stegmented regression model is a discontinuous two-phase regression approach, specifically designed to identify abrupt shifts in linear relationships. The likelihood ratio test was applied to compare the stegmented regression model with the simple linear regression model, in order to evaluate whether the introduction of the breakpoint significantly improved model fit and thereby assess the statistical significance of the breakpoint. The same procedure was used to detect the breakpoint in the relationship between M intensity and drought propagation time. For the M–S–E and M–E–S pathways, the propagation time was defined as the average of the time lags between M and S and between M and E. We used bin medians to detect breakpoints, both to manage the extremely large data size and its computational burden, and to filter noise while highlighting the main trends[56,57]. Therefore, the detected breakpoints represent the major transitions in the average responses of drought propagation characteristics to increasing M intensity. Sensitivity tests of bin number were performed. In addition to M intensity, cumulative P deficit and cumulative PET surplus were also used to detect breakpoints. Cumulative P deficit was calculated as the negative sum of de-trended P during M, whereas cumulative PET surplus was calculated as the sum of de-trended PET during M; both were standardized by the SDs of their respective de-trended series.

The mean ecohydrological damage per unit M intensity, averaged across the four pathways, was calculated for each pixel. Moreover, AC1

values of PPET, SM, and LAI were used to represent atmospheric adjustment capability, soil resilience, and vegetation resilience (the capacity to maintain stability and recover from disturbance), respectively, with higher AC1 indicating weaker adjustment capability and resilience[29,31]. Taking PPET as an example, AC1 was calculated by fitting an autoregressive model as shown in Eq. (1)[30]. Spearman correlations were applied to examine the relationships between resilience, drought propagation time, and ecohydrological damage.

$$\mathrm{PPET}_{t+1} = \mathrm{AC1} \cdot \mathrm{PPET}_t + \varepsilon_t \quad (1)$$

where PPET_{t+1} and PPET_t are the values of de-trended PPET at times $t+1$ and t, respectively, and ε_t is the regression error.

Meteorological drivers of drought propagation

Convergent cross mapping (CCM) is an effective method for detecting causal relationships in time series from complex systems, especially those with non-separability and weak-to-moderate variable coupling[58]. Building on time-delay embedding theory, the value of a variable at a given time, together with its past values, defines a point in a high-dimensional space; as time evolves, the point traces out the shadow manifold. CCM constructs shadow manifolds from time series of a driver variable and a response variable, and then evaluates their topological correspondence[17,58]. The strength of causality is quantified by cross-mapping skill, which reflects how reliably the historical records of the driver variable can predict the state of the response variable in the reconstructed phase space. The CCM in this study was done by using the causal-ccm package in Python[58,59].

However, spurious causality may be detected when variables are affected synchronously. To overcome this interference, the time-lagged CCM introduces a temporal offset between the driver variable and the response variable, and calculates the cross-mapping skills at varying temporal offsets[9]. In this study, we adopted the time-lagged CCM to quantify the response lag and propagation efficiency from P and PET to SM and LAI (i.e., P → SM, PET → SM, P → LAI and PET → LAI). By testing lag parameters ranging from 0 to 11 months, the response lag between each variable pair in each climatic zone was defined as the time lag that maximized the cross-mapping skill, while applying a penalty factor of 1.1 to avoid overestimation of lag (i.e., selecting a longer lag only if the improvement in skill exceeds 10%).

The propagation efficiency between each variable pair for each pixel was computed as the cross-mapping skill based on the time-lagged CCM and the corresponding response lag, where values closer to 1 indicate more efficient propagation between variables. For comparative analysis of propagation efficiency across different variable pairs, we developed an index of relative propagation efficiency as follows:

$$\rho(\mathrm{P} \to \mathrm{SM} \mid \mathrm{PET} \to \mathrm{SM}) = \frac{1-\rho(\mathrm{PET} \to \mathrm{SM})}{1-\rho(\mathrm{P} \to \mathrm{SM})} - 1 \quad (2)$$

where P → SM and PET → SM denote the propagation from P to SM and from PET to SM, respectively. $\rho(\mathrm{P} \to \mathrm{SM} \mid \mathrm{PET} \to \mathrm{SM})$ is the relative propagation efficiency of P → SM compared to PET → SM. $\rho(\mathrm{P} \to \mathrm{SM})$ and $\rho(\mathrm{PET} \to \mathrm{SM})$ are the propagation efficiencies of P → SM and PET → SM, respectively, with values closer to 1 indicating more efficient propagation. $\rho(\mathrm{P} \to \mathrm{SM} \mid \mathrm{PET} \to \mathrm{SM}) > 0$ indicates that P → SM is more efficiently propagated than PET → SM, whereas $\rho(\mathrm{P} \to \mathrm{SM} \mid \mathrm{PET} \to \mathrm{SM}) < 0$ indicates the opposite case.

To visualize the variation in relative propagation efficiency across the climatic gradient, the data were sorted into $\sqrt{n}/2$ bins (rounded to the nearest integer), where n is the length of data, according to the ascending order of aridity index. Within each bin, median values were calculated, and a smoothed curve of relative propagation efficiency and aridity index was generated using Smoothing Splines. Its 95% confidence interval was estimated using the bootstrapped method with 1000 replications.

Partial correlation analysis was employed to further investigate the underlying physical drivers of PET, including air temperature, net radiation, relative humidity, and wind speed.

Modulation of drought propagation by soil–vegetation feedbacks

For the drought propagation of M–S–E, partial correlation analysis was employed to explore the relationship between antecedent SM (defined as SM between the onset of S and E) and the intensity of E, while controlling for the intensity of M. Similarly, for the drought propagation of M–E–S, we assessed the relationship between antecedent LAI (defined as LAI between the onset of E and S) and the intensity of S based on the same method.

To further evaluate the role of soil–vegetation feedbacks, we conducted a mediation analysis, which tests whether the effect of an independent variable on a dependent variable is transmitted through a third, mediating variable. For the M–S–E pathway, the independent variable was the sum of de-trended P during M, the mediating variable was antecedent SM, and the dependent variable was the sum of de-trended LAI during E. For the M–E–S pathway, the independent variable was the sum of de-trended PET during M, the mediating variable was antecedent LAI, and the dependent variable was the sum of de-trended SM during S. Each variable was standardized by the SD of its respective detrended series. For each case, mediation analysis based on linear regressions was performed to examine (1) the effect of the independent variable on the mediating variable; (2) the total effect of the independent variable on the dependent variable; and (3) the direct and mediation effects of the independent variable on the dependent variable. These effects were quantified using the mediation package in R[60]. Non-parametric bootstrapping with 1000 replications was employed to assess the statistical significance of the effects.

Based on the onset timing of M, drought propagation events were classified into four seasons: March–May (spring), June–August (summer), September–November (autumn), and December–February of the following year (winter) in the Northern Hemisphere, and vice versa in the Southern Hemisphere. Seasonal variations in drought propagation were subsequently quantified.

Reporting summary

Further information on research design is available in the Nature Portfolio Reporting Summary linked to this article.

Data availability

All datasets used in this study are publicly available. CRU TS data can be accessed at: https://crudata.uea.ac.uk/cru/data/hrg/. GLEAM data can be accessed at: https://www.gleam.eu/. GIMMS LAI4g data can be accessed at: https://zenodo.org/records/8281930. Aridity index data can be accessed at: https://doi.org/10.6084/m9.figshare.7504448. BESSv2.0 GPP and NEE can be accessed at: https://www.environment.snu.ac.kr/data/. RTSIF can be accessed at: https://doi.org/10.6084/m9.figshare.19336346. ERA5-Land data can be accessed at: https://cds.climate.copernicus.eu/datasets/reanalysis-era5-land-monthly-means?tab=overview.

Code availability

All analyses were conducted using publicly available function or packages in MATLAB, Python, and R: the chngpt package is available at https://github.com/cran/chngpt[55]; the causal_ccm package is available at https://github.com/PrinceJavier/causal_ccm[59]; the mediation package is available at https://github.com/kosukeimai/mediation[60]; the detrend function is available at https://ww2.mathworks.cn/help/matlab/ref/detrend.html.

Received: 7 October 2025; Accepted: 12 February 2026;
Published online: 27 February 2026

References

1. Ahmad, D. M. & Kam, J. Disparity between global drought hazard and awareness. *npj Clean Water* **7**, https://doi.org/10.1038/s41545-024-00373-y (2024).

2. UNDRR. *GAR Special Report on Drought 2021: Summary for Policymakers*. https://www.undrr.org/publication/gar-special-report-drought-2021 (United Nations Office for Disaster Risk Reduction, 2021).
3. Dai, A. G. Increasing drought under global warming in observations and models. *Nat. Clim. Change* **3**, 52–58 (2013).
4. Fuentes, I., Padarian, J. & Vervoort, R. W. Spatial and temporal global patterns of drought propagation. *Front. Environ. Sci.* **10**, https://doi.org/10.3389/fenvs.2022.788248 (2022).
5. Stocker, B. D. et al. Drought impacts on terrestrial primary production underestimated by satellite monitoring. *Nat. Geosci.* **12**, 264 (2019).
6. Entekhabi, D. Propagation in the drought cascade: Observational analysis over the continental US. *Water Resour. Res.* **59**, https://doi.org/10.1029/2022wr032608 (2023).
7. Mukherjee, S., Mishra, A. K., Zscheischler, J. & Entekhabi, D. Interaction between dry and hot extremes at a global scale using a cascade modeling framework. *Nat. Commun.* **14**, https://doi.org/10.1038/s41467-022-35748-7 (2023).
8. Mishra, A. K. & Singh, V. P. A review of drought concepts. *J. Hydrol.* **391**, 204–216 (2010).
9. Wang, H. et al. Study on the multi-type drought propagation process and driving factors on the Tibetan Plateau. *J. Hydrol.* **645**, https://doi.org/10.1016/j.jhydrol.2024.132162 (2024).
10. Geng, G., Zhang, B., Gu, Q., He, Z. & Zheng, R. Drought propagation characteristics across China: time, probability, and threshold. *J. Hydrol.* **631**, https://doi.org/10.1016/j.jhydrol.2024.130805 (2024).
11. Wu, G. et al. Impacts of global climate warming on meteorological and hydrological droughts and their propagations. *Earths Future* **10** https://doi.org/10.1029/2021ef002542 (2022).
12. Chen, L. et al. Global increase in the occurrence and impact of multiyear droughts. *Science* **387**, 278–284 (2025).
13. Gampe, D. et al. Increasing impact of warm droughts on northern ecosystem productivity over recent decades. *Nat. Clim. Change* **11**, 772 (2021).
14. Phillips, O. L. et al. Drought sensitivity of the Amazon rainforest. *Science* **323**, 1344–1347 (2009).
15. Crausbay, S. D. et al. Defining ecological drought for the twenty-first century. *Bull. Am. Meteorol. Soc.* **98**, 2543–2550 (2017).
16. Zhang, L. et al. Ecological drought evolution characteristics under different climatic regions in the Yangtze River basin. *J. Hydrol.* **629** https://doi.org/10.1016/j.jhydrol.2023.130573 (2024).
17. Zhou, Z. et al. Recent development on drought propagation: A comprehensive review. *J. Hydrol.* **645**, https://doi.org/10.1016/j.jhydrol.2024.132196 (2024).
18. Zhu, Y., Liu, Y., Wang, W., Singh, V. P. & Ren, L. L. A global perspective on the probability of propagation of drought: From meteorological to soil moisture. *J. Hydrol.* **603**, https://doi.org/10.1016/j.jhydrol.2021.126907 (2021).
19. Sungmin, O. & Park, S. K. Global ecosystem responses to flash droughts are modulated by background climate and vegetation conditions. *Commun. Earth Environ.* **5**, https://doi.org/10.1038/s43247-024-01247-4 (2024).
20. Seneviratne, S. I. et al. Investigating soil moisture-climate interactions in a changing climate: a review. *Earth-Sci. Rev.* **99**, 125–161 (2010).
21. Yuan, X. et al. A global transition to flash droughts under climate change. *Science* **380**, 187–191 (2023).
22. Yang, H., Ma, F., Yuan, X., Ji, P. & Li, C. Vegetation greening accelerated the propagation from meteorological to soil droughts in the Loess Plateau from a three-dimensional perspective. *J. Hydrol.* **650**, https://doi.org/10.1016/j.jhydrol.2024.132522 (2025).
23. Prieto, I., Armas, C. & Pugnaire, F. I. Water release through plant roots: new insights into its consequences at the plant and ecosystem level. *New Phytologist* **193**, 830–841 (2012).
24. Kim, J. & Mohanty, B. P. Influence of lateral subsurface flow and connectivity on soil water storage in land surface modeling. *J. Geophys. Res.* **121**, 704–721 (2016).
25. Zhou, Z. et al. Assessing the soil moisture-vegetation mutual feedback relationship in different climatic regions of mainland China. *Catena* **249**, https://doi.org/10.1016/j.catena.2024.108684 (2025).
26. Yang, C., Liu, C., Xing, X. & Ma, X. Predicting the risk and trigger thresholds for propagation of meteorological droughts to agricultural droughts in China based on Copula-Bayesian model. *Agric. Water Manag.* **313**, https://doi.org/10.1016/j.agwat.2025.109468 (2025).
27. Huang, S. et al. The propagation from meteorological to hydrological drought and its potential influence factors. *J. Hydrol.* **547**, 184–195 (2017).
28. Forzieri, G., Dakos, V., McDowell, N. G., Ramdane, A. & Cescatti, A. Emerging signals of declining forest resilience under climate change. *Nature* **608**, 534 (2022).
29. Smith, T., Traxl, D. & Boers, N. Empirical evidence for recent global shifts in vegetation resilience. *Nat. Clim. Change* **12**, 477 (2022).
30. Yao, Y. et al. Declined terrestrial ecosystem resilience. *Global Change Biol.* **30**, https://doi.org/10.1111/gcb.17291 (2024).
31. Smith, T. & Boers, N. Global vegetation resilience linked to water availability and variability. *Nat. Commun.* **14**, https://doi.org/10.1038/s41467-023-36207-7 (2023).
32. Dai, A., Zhao, T. & Chen, J. Climate change and drought: A precipitation and evaporation perspective. *Curr. Clim. Change Rep.* **4**, 301–312 (2018).
33. Zhu, S., Huang, W., Wei, Y., Guo, J. & Qin, H. Impact of driving factors on drought propagation: perspectives on rainfall deficit and excessive evaporation. *Climate Dyn.* **63**, https://doi.org/10.1007/s00382-025-07618-7 (2025).
34. Cai, G. C., Ahmed, M. A., Abdalla, M. & Carminati, A. Root hydraulic phenotypes impacting water uptake in drying soils. *Plant Cell Environ.* **45**, 650–663 (2022).
35. Dubbert, M. & Werner, C. Water fluxes mediated by vegetation: emerging isotopic insights at the soil and atmosphere interfaces. *New Phytologist* **221**, 1754–1763 (2019).
36. Chiang, F., Mazdiyasni, O. & AghaKouchak, A. Evidence of anthropogenic impacts on global drought frequency, duration, and intensity. *Nat. Commun.* **12**, https://doi.org/10.1038/s41467-021-22314-w (2021).
37. Trenberth, K. E. et al. Global warming and changes in drought. *Nat. Clim. Change* **4**, 17–22 (2014).
38. Harris, I., Osborn, T. J., Jones, P. & Lister, D. Version 4 of the CRU TS monthly high-resolution gridded multivariate climate dataset. *Sci. Data* **7**, https://doi.org/10.1038/s41597-020-0453-3 (2020).
39. Liski, J., Nissinen, A., Erhard, M. & Taskinen, O. Climatic effects on litter decomposition from arctic tundra to tropical rainforest. *Glob. Change Biol.* **9**, 575–584 (2003).
40. Miralles, D. G. et al. GLEAM4: global land evaporation and soil moisture dataset at 0.1° resolution from 1980 to near present. *Sci. Data* **12**, 416 (2025).
41. Cao, S. et al. Spatiotemporally consistent global dataset of the GIMMS Leaf Area Index (GIMMS LAI4g) from 1982 to 2020 (V1.2). Zenodo https://doi.org/10.5281/zenodo.8281930 (2023).
42. Cao, S. et al. Spatiotemporally consistent global dataset of the GIMMS leaf area index (GIMMS LAI4g) from 1982 to 2020. *Earth Syst. Sci. Data* **15**, 4877–4899 (2023).
43. Li, B. L. et al. BESSv2.0: a satellite-based and coupled-process model for quantifying long-term global land-atmosphere fluxes. *Remote Sens. Environ.* **295**, https://doi.org/10.1016/j.rse.2023.113696 (2023).
44. Chen, X. A. et al. A long-term reconstructed TROPOMI solar-induced fluorescence dataset using machine learning algorithms. *Sci. Data* **9**, https://doi.org/10.1038/s41597-022-01520-1 (2022).
45. Chen, X. A. et al. A long-term reconstructed TROPOMI solar-induced fluorescence dataset using machine learning algorithms. figshare https://doi.org/10.6084/m9.figshare.19336346 (2022).

46. Munoz-Sabater, J. et al. ERA5-Land: a state-of-the-art global reanalysis dataset for land applications. *Earth Syst. Sci. Data* **13**, 4349–4383 (2021).
47. Muñoz Sabater, J. *ERA5-Land Monthly Averaged Data from 1950 to Present*. https://doi.org/10.24381/cds.68d2bb30 (*Copernicus Climate Change Service (C3S) Climate Data Store (CDS)*, 2019).
48. Yuan, W. P. et al. Increased atmospheric vapor pressure deficit reduces global vegetation growth. *Sci. Adv.* **5**, https://doi.org/10.1126/sciadv.aax1396 (2019).
49. Zomer, R. J., Xu, J. & Trabucco, A. Version 3 of the global aridity index and potential evapotranspiration database. *Sci. Data* **9**, https://doi.org/10.1038/s41597-022-01493-1 (2022).
50. Zomer, R. J. & Trabucco, A. Global Aridity Index and Potential Evapotranspiration (ET0) climate database. figshare https://doi.org/10.6084/m9.figshare.7504448 (2019).
51. Liu, Y. et al. Drought legacies delay spring green-up in northern ecosystems. *Nat. Climate Change* **15**, https://doi.org/10.1038/s41558-025-02273-6 (2025).
52. Crausbay, S. D. et al. Unfamiliar territory: Emerging themes for ecological drought research and management. *One Earth* **3**, 337–353 (2020).
53. Kashyap, R., Kuttippurath, J. & Patel, V. K. Ecological droughts increased in India with changing Indian summer monsoon and human interventions. *Commun. Earth Environ.* **6**, https://doi.org/10.1038/s43247-025-02694-3 (2025).
54. Li, C. et al. Climatic driving mechanisms of the propagation from meteorological drought to agricultural and ecological droughts. *J. Environ. Manag.* **383**, https://doi.org/10.1016/j.jenvman.2025.125445 (2025).
55. Fong, Y. Y., Huang, Y., Gilbert, P. B. & Permar, S. R. chngpt: threshold regression model estimation and inference. *BMC Bioinform.* **18**, https://doi.org/10.1186/s12859-017-1863-x (2017).
56. Zhong, Z. Q. et al. Disentangling the effects of vapor pressure deficit on northern terrestrial vegetation productivity. *Sci. Adv.* **9**, https://doi.org/10.1126/sciadv.adf3166 (2023).
57. Feldman, A. F. et al. Large global-scale vegetation sensitivity to daily rainfall variability. *Nature* **636**, 380–384 (2024).
58. Sugihara, G. et al. Detecting causality in complex ecosystems. *Science* **338**, 496–500 (2012).
59. Javier, P. J. E. *causal-ccm a Python implementation of Convergent Cross Mapping [Computer software]. GitHub*, https://github.com/PrinceJavier/causal_ccm (2021).
60. Tingley, D., Yamamoto, T., Hirose, K., Keele, L. & Imai, K. Mediation: R package for causal mediation analysis. *J. Stat. Softw.* **59**, (2014).
61. Jiang, S. et al. Generic Diagramming Platform (GDP): a comprehensive database of high-quality biomedical graphics. *Nucleic Acids Res.* **53**, D1670–D1676 (2024).

Acknowledgements

This research was financially supported by the National Natural Science Foundation of China (42521001), the Fundamental and Interdisciplinary Disciplines Breakthrough Plan of the Ministry of Education of China (JYB2025XDXIM901), the China Scholarship Council (CSC), the Talents Incubation Project of School of Natural Resources at Beijing Normal University (2024YC06) and the Tsinghua University (100008001).

Author contributions

Z.Q.: Conceptualization, Data curation, Formal analysis, Investigation, Methodology, Software, Validation, Visualization, Writing – original draft. X.L.: Conceptualization, Funding acquisition, Project administration, Writing – review & editing. J.P.: Investigation, Writing – review & editing. D.C.: Investigation, Writing – review & editing. C.M.: Investigation, Writing – review & editing. Y.D.: Investigation, Writing – review & editing. F.S.: Investigation, Writing – review & editing. W.L.: Investigation, Writing – review & editing.

Competing interests

The authors declare no competing interests.

Additional information

Supplementary information The online version contains supplementary material available at https://doi.org/10.1038/s43247-026-03330-4.

Correspondence and requests for materials should be addressed to Xiaoyan Li.

Peer review information *Communications Earth and Environment* thanks the anonymous reviewers for their contribution to the peer review of this work. Primary Handling Editors: Yangxiaoyue Liu and Nicola Colombo. [A peer review file is available.]

Reprints and permissions information is available at http://www.nature.com/reprints

Publisher's note Springer Nature remains neutral with regard to jurisdictional claims in published maps and institutional affiliations.

Open Access This article is licensed under a Creative Commons Attribution-NonCommercial-NoDerivatives 4.0 International License, which permits any non-commercial use, sharing, distribution and reproduction in any medium or format, as long as you give appropriate credit to the original author(s) and the source, provide a link to the Creative Commons licence, and indicate if you modified the licensed material. You do not have permission under this licence to share adapted material derived from this article or parts of it. The images or other third party material in this article are included in the article's Creative Commons licence, unless indicated otherwise in a credit line to the material. If material is not included in the article's Creative Commons licence and your intended use is not permitted by statutory regulation or exceeds the permitted use, you will need to obtain permission directly from the copyright holder. To view a copy of this licence, visit http://creativecommons.org/licenses/by-nc-nd/4.0/.

© The Author(s) 2026